10.2514/6.2023-1244

High-Fidelity CFD Verification Workshop 2024: Spalart-Allmaras QCR2000-R Turbulence Model

Boris Diskin[1] and Yi Liu[2]
National Institute of Aerospace, Hampton, Virginia 23666, USA

Marshall C. Galbraith[3]
Massachusetts Institute of Technology, Massachusetts 03130, USA

This is an invited paper for the SciTech 2023 special session, High-Fidelity CFD Verification Preworkshop. The paper presents three test cases for verification of Reynolds-averaged Navier-Stokes solvers. The verification studies focus on a one-equation Spalart-Allmaras model, SA-neg-QCR2000-R. The test cases are a two-dimensional subsonic flow around a Joukowski airfoil, a subsonic three-dimensional flow around an extruded NACA 0012 wing in a tunnel, and a subsonic flow around a wing-body configuration developed by Boeing for verification of solvers participating in the High-Lift Prediction Workshop. The turbulence-model formulation, geometry, flow conditions, grids, and the desired outcome are described in detail. Solutions for the test cases computed by established codes are shown.

I. Introduction

A High-Fidelity Computational Fluid Dynamics Verification Workshop (HFCFDVW) is planned at the American Institute of Aeronautics and Astronautics (AIAA) SciTech Forum in 2024 to verify computational fluid dynamics (CFD) approaches to simulation of steady and unsteady turbulent flows. HFCFDVW is a successor to a series of workshops and special sessions that have been supported by AIAA for a number of years. These preceding activities include the High-Fidelity CFD Workshop [1], conducted at the AIAA SciTech Forum in 2022, a series of AIAA special sessions and international workshops on high-order methods (see, e.g., Refs. [2, 3]), and a series of AIAA special sessions and publications on Reynolds-averaged Navier-Stokes (RANS) solver technology [4, 5]. This year, a special session is organized at the AIAA SciTech 2023 Forum to lay the groundwork for the HFCFDVW. This special session introduces test suites for verification of CFD codes through comparison of simulations conducted by different codes using well-defined verification metrics. In distinction from validation studies that focus on the ability of model equations to represent correct physical behavior, verification studies focus on correctness of implementation of specific models. Four test suites have been identified for verification of wall-modeled large-eddy simulations, mesh motion, simulations of shock-dominated flows, and RANS simulations of separating flows. The special session is expected to facilitate formation of working groups to collaborate during the next year on establishing best verification practices for the test suites. At HFCFDVW, each group will report on the verification studies and present findings and recommendations.

This paper presents three test cases suggested by the HFCFDVW organizing committee for verification of RANS solvers. The target model is a one-equation Spalart-Allmaras (SA) model [6] that uses quadratic constitutive relation (QCR) [7] and a simple rotation correction proposed in Refs. [8, 9]. The negative variant [10] of the SA model is recommended due to its superior numerical behavior. The model is referred to as SA-neg-QCR2000-R according to the naming convention of the NASA turbulence-modeling resource (TMR) website [11]. The QCR is needed for SA-based RANS simulations of corner flows because normal stress differences induce flowfield behavior that cannot be captured with linear eddy-viscosity models that

[1]Senior Research Fellow, Associate Fellow AIAA
[2]Associate Principal Research Engineer, Senior Member AIAA
[3]Research Engineer, Department of Aeronautics & Astronautics, Senior Member AIAA

make use of the Boussinesq assumption. The rotation correction designated as –R is a specific modification that intends to mitigate generation of spurious eddy viscosity within a mature vortex. In preparation for this paper and HFCFDVW, a small group of researchers that included the authors of the SA model, the authors of the paper, and some other researchers, discussed clarifications on implementation of the –R correction in the positive and negative variants of the SA model. The results of these discussions have been reflected on the TMR website and are summarized in the paper.

The three test cases include a two-dimensional (2D) flow around a Joukowski airfoil, a three-dimensional (3D) internal flow around an extruded NACA 0012 wing in a tunnel, and a 3D flow around a simplified wing-body high-lift common research model (CRM-HL-WB) developed by Boeing for verification of CFD solvers applied to high-lift aerodynamics research. In this paper, solutions for each case are computed using well established RANS solvers to provide example computations for workshop participants. Families of consistently refined unstructured grids have been generated for each case and will be available to the community through the HFCFDVW website [12]. To minimize grid effects on solver verification, it is recommended to conduct simulations on the grids provided by the workshop. Iterative convergence to low (ideally, machine-zero) levels of residuals is expected on all grids.

The material in the paper is presented in the following order. The RANS equations and the SA-neg-QCR2000-R turbulence model are described in detail in Section II. Section III briefly introduces solvers used for computing test-case solutions. Sections IV, V, and VI describe the three test cases and the corresponding solutions. Concluding remarks are given in Section VII.

II. Reynolds-Averaged Navier-Stokes Equations

The three-dimensional compressible unsteady RANS equations are given in Ref. [13].

$$\partial_t \boldsymbol{Q} + \partial_x \boldsymbol{F} + \partial_y \boldsymbol{G} + \partial_z \boldsymbol{H} = \boldsymbol{0} \tag{1}$$

The vectors $\boldsymbol{F}$, $\boldsymbol{G}$, and $\boldsymbol{H}$ are defined in Eq. 2.

$$\boldsymbol{F} = \begin{pmatrix} \rho u \\ \rho uu + p - \tau_{xx} \\ \rho uv - \tau_{xy} \\ \rho uw - \tau_{xz} \\ (E+p)u - \left(u\tau_{xx} + v\tau_{xy} + w\tau_{xz}\right) + q_x \end{pmatrix}$$

$$\boldsymbol{G} = \begin{pmatrix} \rho v \\ \rho uv - \tau_{xy} \\ \rho vv + p - \tau_{yy} \\ \rho vw - \tau_{yz} \\ (E+p)v - \left(u\tau_{xy} + v\tau_{yy} + w\tau_{yz}\right) + q_y \end{pmatrix} \tag{2}$$

$$\boldsymbol{H} = \begin{pmatrix} \rho w \\ \rho uw - \tau_{xz} \\ \rho vw - \tau_{yz} \\ \rho ww + p - \tau_{zz} \\ (E+p)w - \left(u\tau_{xz} + v\tau_{yz} + w\tau_{zz}\right) + q_z \end{pmatrix}$$

Here, p is the static pressure, $\boldsymbol{u} = (u, v, w)^{\mathrm{T}}$ is the velocity vector, $\boldsymbol{q} = \left(q_x, q_y, q_z\right)^{\mathrm{T}}$ is the local heat flux vector, and $\boldsymbol{Q} \equiv (\rho, \rho u, \rho v, \rho w, E)^{\mathrm{T}}$ is the vector of conserved variables that includes the density ρ, the momentum $\rho\boldsymbol{u} = (\rho u, \rho v, \rho w)^{\mathrm{T}}$, and the total energy per unit volume E. The superscript T denotes transposition to indicate column vectors. The vector of primitive variables is $(\rho, u, v, w, p)^{\mathrm{T}}$. For a perfect gas, equations are closed using the relations defined in Eq. 3.

$$p = (\gamma - 1)\left(E - \frac{\rho}{2}(u^2 + v^2 + w^2)\right), \qquad T = a^2 = \gamma\frac{p}{\rho} \tag{3}$$

Here, T is the local temperature, a is the speed of sound, and $\gamma = 1.4$ is the ratio of specific heats.

The viscous fluxes in the RANS equations refer to the diffusion terms including the shear stress tensor and the heat flux vector as defined in Eq. 4.

$$\begin{aligned}
\tau_{xx} &= \frac{2}{3}(\mu+\mu_t)\left(2\partial_x u - \partial_y v - \partial_z w\right) \\
\tau_{yy} &= \frac{2}{3}(\mu+\mu_t)\left(2\partial_y v - \partial_x u - \partial_z w\right) \\
\tau_{zz} &= \frac{2}{3}(\mu+\mu_t)\left(2\partial_z w - \partial_x u - \partial_y v\right) \\
\tau_{yx} &= \tau_{xy} = (\mu+\mu_t)\left(\partial_x v + \partial_y u\right) \\
\tau_{zx} &= \tau_{xz} = (\mu+\mu_t)(\partial_x w + \partial_z u) \\
\tau_{zy} &= \tau_{yz} = (\mu+\mu_t)\left(\partial_z v + \partial_y w\right) \\
q_x &= \frac{1}{(\gamma-1)}\left(\frac{\mu}{Pr} + \frac{\mu_t}{Pr_t}\right)\partial_x T \\
q_y &= \frac{1}{(\gamma-1)}\left(\frac{\mu}{Pr} + \frac{\mu_t}{Pr_t}\right)\partial_y T \\
q_z &= \frac{1}{(\gamma-1)}\left(\frac{\mu}{Pr} + \frac{\mu_t}{Pr_t}\right)\partial_z T
\end{aligned} \tag{4}$$

Here, μ is the dynamic laminar viscosity computed by Sutherland's law [14], μ_t is the turbulent eddy viscosity computed by a turbulence model, and $Pr = 0.72$ and $Pr_t = 0.9$ are the Prandtl numbers for the meanflow and turbulence models, respectively. In Sutherland's law, the local dynamic viscosity, μ, relates to the local temperature, T, through Eq. 5.

$$\mu = \mu_{ref}\left(\frac{T}{T_{ref}}\right)^{\frac{3}{2}}\left(\frac{T_{ref}+S^*}{T+S^*}\right) \tag{5}$$

Here, $S^* = 198.6$ °R and the reference viscosity, μ_{ref}, is assumed at the reference temperature T_{ref}.

Following the formulation presented at the TMR website [11], the standard Spalart-Allmaras (SA) turbulence model [6] is given by Eq. 6.

$$\partial_t \hat{\nu} + \boldsymbol{u}\cdot\boldsymbol{\nabla}\hat{\nu} - c_{b1}(1-f_{t2})\hat{S}\hat{\nu} + \left[c_{w1}f_w - \frac{c_{b1}}{\kappa^2}f_{t2}\right]\left(\frac{\hat{\nu}}{d}\right)^2 - \frac{1}{\sigma}\left[\boldsymbol{\nabla}\cdot\left((\nu+\hat{\nu})\boldsymbol{\nabla}\hat{\nu}\right) + c_{b2}(\boldsymbol{\nabla}\hat{\nu}\cdot\boldsymbol{\nabla}\hat{\nu})\right] = 0 \tag{6}$$

Here, $\boldsymbol{\nabla} \equiv \left(\partial_x, \partial_y, \partial_z\right)^{\mathrm{T}}$ denotes a formal vector of spatial derivatives. The boundary conditions are defined in Eq. 7.

$$\hat{\nu}_{wall} = 0, \qquad \hat{\nu}_{farfield} = 3\nu_{ref} \tag{7}$$

Here, $\hat{\nu}$ is the turbulence variable, d is the distance to the nearest wall, including a tangency wall (perfect slip inviscid boundary conditions), $\nu = \mu/\rho$ is the kinematic viscosity, and ν_{ref} is the reference kinematic viscosity. The turbulent eddy viscosity is computed as in Eq. 8.

$$\mu_t = \rho\hat{\nu}f_{v1} \tag{8}$$

In the original reference [6], the term $\hat{S}$ is defined as follows.

$$\hat{S} = \Omega + \bar{\mathrm{S}}, \qquad \bar{\mathrm{S}} = \frac{\hat{\nu}}{\kappa^2 d^2}f_{v2} \tag{9}$$

Here, Ω is the magnitude of vorticity defined in Eq. 10.

$$\Omega = \sqrt{\left(\partial_y w - \partial_z v\right)^2 + (\partial_z u - \partial_x w)^2 + \left(\partial_x v - \partial_y u\right)^2} \tag{10}$$

To avoid numerical problems associated with $\hat{S} \le 0$, Ref. [10] suggests the following modification.

$$\hat{S} = \Omega + \frac{\Omega(c_2^2\Omega + c_3\bar{\mathrm{S}})}{(c_3 - 2c_2)\Omega - \bar{\mathrm{S}}} \quad \text{when} \quad \bar{\mathrm{S}} < -c_2\Omega, \quad c_2 = 0.7, \qquad c_3 = 0.9 \tag{11}$$

Other terms appearing in Eq. 6 are defined as follows.

$$f_{v1} = \frac{\chi^3}{c_{v1}^3 + \chi^3}, \ \chi = \frac{\hat{\nu}}{\nu}, \ f_{v2} = 1 - \frac{\chi}{1 + \chi f_{v1}}, \ f_w = g\left[\frac{1 + c_{w3}^6}{g^6 + c_{w3}^6}\right]^{\frac{1}{6}}, \ g = r + c_{w2}(r^6 - r),$$
$$f_{t2} = c_{t3}\exp(-c_{t4}\chi^2), \ r = \min\left[\frac{\hat{\nu}}{\hat{S}\kappa^2 d^2}, 10\right] \tag{12}$$

The constants are $\kappa = 0.41$, $\sigma = \frac{2}{3}$, $c_{b1} = 0.1355$, $c_{b2} = 0.622$, $c_{t3} = 1.2$, $c_{t4} = 0.5$, $c_{v1} = 7.1$, $c_{w1} = \frac{c_{b1}}{\kappa} + \frac{1+c_{b2}}{\sigma}$, $c_{w2} = 0.3$, and $c_{w3} = 2$.

The standard SA model equation requires $\hat{\nu} > 0$. The SA model extended to negative values of $\hat{\nu}$ is referred to as the SA-neg model [10]. For negative $\hat{\nu}$, Eq. 13 is solved.

$$\partial_t\hat{\nu} + \boldsymbol{u}\cdot\boldsymbol{\nabla}\hat{\nu} - c_{b1}(1 - c_{t3})\Omega\hat{\nu} - c_{w1}\left(\frac{\hat{\nu}}{d}\right)^2 - \frac{1}{\sigma}\left[\boldsymbol{\nabla}\cdot\left((\nu + \hat{\nu}f_n)\boldsymbol{\nabla}\hat{\nu}\right) + c_{b2}(\boldsymbol{\nabla}\hat{\nu}\cdot\boldsymbol{\nabla}\hat{\nu})\right] = 0 \tag{13}$$

Function f_n is defined in Eq. 14.

$$f_n = \frac{c_{n1} + \chi^3}{c_{n1} - \chi^3}, \qquad c_{n1} = 16 \tag{14}$$

The SA-neg turbulent eddy viscosity is computed using Eq. 8 when $\hat{\nu} \ge 0$ and set to zero when $\hat{\nu} < 0$.

In the SA-R variant of the turbulence model with a rotational correction [8, 9], the production term of the SA model, Eq. 6, is modified, resulting in the model given by Eq. 15.

$$\partial_t\hat{\nu} + \boldsymbol{u}\cdot\boldsymbol{\nabla}\hat{\nu} - c_{b1}(1 - f_{t2})\big(\hat{S} + \mathrm{c_{rot}}\min(0, S - \Omega)\big)\hat{\nu}$$
$$+ \left[c_{w1}f_w - \frac{c_{b1}}{\kappa^2}f_{t2}\right]\left(\frac{\hat{\nu}}{d}\right)^2 - \frac{1}{\sigma}\left[\boldsymbol{\nabla}\cdot\left((\nu + \hat{\nu})\boldsymbol{\nabla}\hat{\nu}\right) + c_{b2}(\boldsymbol{\nabla}\hat{\nu}\cdot\boldsymbol{\nabla}\hat{\nu})\right] = 0 \tag{15}$$

Here, the strain magnitude, S, is defined as in Eq. 16.

$$S = \sqrt{\left(\partial_y w + \partial_z v\right)^2 + (\partial_z u + \partial_x w)^2 + \left(\partial_x v + \partial_y u\right)^2 + 2(\partial_x u)^2 + 2\left(\partial_y v\right)^2 + 2(\partial_z w)^2} \tag{16}$$

If the strain magnitude is less than the vorticity magnitude, $S < \Omega$, and $c_{rot} > 1$, the production term may become negative and suppress production of eddy viscosity, which is considered as a desirable property in case of a solid body rotation. References [8, 9] recommend $c_{rot} = 2$. Computations reported in Ref. [15] use $c_{rot} = 1$. Note that all models based on SA-neg [10] benefit from smooth transition through $\hat{\nu} = 0$; therefore, it would be preferable to have the production term as $c_{b1}(1 - c_{t3})(\Omega + c_{rot}\min(0, S - \Omega))\hat{\nu}$ in the negative branch of the SA-neg-R model. On the other hand, SA-neg does not allow a negative production term for $\hat{\nu} < 0$. For the current verification campaign, the negative branch uses the absolute value of the preferable production term.

$$\partial_t\hat{\nu} + \boldsymbol{u}\cdot\boldsymbol{\nabla}\hat{\nu} - c_{b1}(1 - c_{t3})\,|\Omega + c_{rot}\min(0, S - \Omega)|\hat{\nu}$$
$$- c_{w1}\left(\frac{\hat{\nu}}{d}\right)^2 - \frac{1}{\sigma}\left[\boldsymbol{\nabla}\cdot\left((\nu + \hat{\nu}f_n)\boldsymbol{\nabla}\hat{\nu}\right) + c_{b2}(\boldsymbol{\nabla}\hat{\nu}\cdot\boldsymbol{\nabla}\hat{\nu})\right] = 0 \tag{17}$$

The mandatory verification is performed for $c_{rot} = 1.0$. This choice ensures positivity of the production term as $\Omega + \min(0, S - \Omega) > 0$ and a smooth transition between the positive and negative branches of the SA-neg-R model. However, it is believed that $c_{rot} = 1.0$ does not sufficiently suppress spurious eddy viscosity. The optional computations are suggested for $c_{rot} = 2.0$. In this scenario, the SA-neg-R production term is only C0 continuous for flow regimes where $\Omega + c_{rot}\min(0, S - \Omega) < 0$.

The turbulent stress tensor, $\boldsymbol{\tau}_t$, is a part of the total shear stress tensor defined in Eq. 4. Formally, the turbulent stress tensor is defined similar to the total stress tensor, with the total coefficient $(\mu + \mu_t)$ replaced as μ_t. In the QCR2000 formulation [7], the turbulent stress tensor is corrected using the normalized antisymmetric rotation tensor that is defined as follows.

$$O_{xx} = O_{yy} = O_{zz} = 0, \;\; O_{xy} = -O_{yx} = \frac{\partial_y u - \partial_x v}{b}, \;\; O_{xz} = -O_{zx} = \frac{\partial_z u - \partial_x w}{b},$$
$$O_{yz} = -O_{zy} = \frac{\partial_z v - \partial_y w}{b} \tag{18}$$

Here, b is the l_2-norm of the velocity gradient tensor defined in Eq. 19.

$$b = \sqrt{(\partial_x u)^2 + \left(\partial_y u\right)^2 + (\partial_z u)^2 + (\partial_x v)^2 + \left(\partial_y v\right)^2 + (\partial_z v)^2 + (\partial_x w)^2 + \left(\partial_y w\right)^2 + (\partial_z w)^2} \tag{19}$$

The rotation tensor is set to be zero when $b = 0$. The QCR turbulent stress tensor is computed as follows

$$\begin{aligned}
\tau_{t,xx,QCR} &= \tau_{t,xx} - 2c_{cr1}\left(O_{xy}\tau_{t,xy} + O_{xz}\tau_{t,xz}\right) \\
\tau_{t,yy,QCR} &= \tau_{t,yy} - 2c_{cr1}\left(O_{yx}\tau_{t,yx} + O_{yz}\tau_{t,yz}\right) \\
\tau_{t,zz,QCR} &= \tau_{t,zz} - 2c_{cr1}\left(O_{zx}\tau_{t,zx} + O_{zy}\tau_{t,zy}\right) \\
\tau_{t,xy,QCR} &= \tau_{t,xy} - c_{cr1}\left(O_{xy}\left(\tau_{t,yy} - \tau_{t,xx}\right) + O_{yz}\tau_{t,xz} + O_{xz}\tau_{t,yz}\right) \\
\tau_{t,xz,QCR} &= \tau_{t,xz} - c_{cr1}\left(O_{xz}\left(\tau_{t,zz} - \tau_{t,xx}\right) + O_{xy}\tau_{t,zy} + O_{zy}\tau_{t,xy}\right) \\
\tau_{t,yz,QCR} &= \tau_{t,yz} - c_{cr1}\left(O_{yz}\left(\tau_{t,zz} - \tau_{t,yy}\right) + O_{yx}\tau_{t,zx} + O_{zx}\tau_{t,yx}\right) \\
c_{cr1} &= 0.3
\end{aligned} \tag{20}$$

The meanflow stress tensor remains unchanged.

III. Computational Fluid Dynamics Codes

A. FUN3D

FUN3D is a node-centered, finite-volume, unstructured-grid RANS solver developed and supported at the NASA Langley Research Center; FUN3D is widely used for high-fidelity analysis and adjoint-based design of complex turbulent flows [16, 17]. Recently FUN3D has been adapted for NVIDIA GPU architectures [18, 19] and demonstrated breakthrough performance for perfect gas and thermochemical nonequilibrium flows [20, 21]. FUN3D solves the governing flow equations on mixed-element grids. The conservation laws are implemented on control volumes that are constructed around grid points using a median-dual partition of the computational domain. The inviscid fluxes are computed using an approximate Riemann solver. Roe's flux-difference splitting scheme [22] is used in the current study. For second-order accuracy, the solution values at the edge medians are obtained by a UMUSCL scheme [23, 24], with unweighted least-squares gradients computed at the nodes. For this study, the UMUSCL scheme with $\kappa = 0.5$ and no gradient limiting is used for the meanflow equations. In these studies, FUN3D uses a first-order nonconservative approximation [10] for the turbulence-model convection term.

The viscous fluxes are discretized using the Green-Gauss (cell-based) gradients. For tetrahedral grids, this approach is equivalent to a finite-element Galerkin-type approximation [25]. On nontetrahedral cells, the edge-based gradients are combined with the Green-Gauss gradients [26, 27]; this approach improves stability of the viscous operator. The diffusion term in the turbulence model is handled in the same fashion as the meanflow viscous terms. The vorticity for the turbulence-model source term is computed using a Green-Gauss approximation on dual cells. The boundary conditions involved in the present study include subsonic inflow, specified back-pressure outflow, farfield Roe-based, farfield Riemann-invariant-based, symmetry, tangency-wall, and strong viscous-wall boundary conditions [16, 28].

B. SANS

Solution Adaptive Numerical Simulator (SANS) [29], currently under development at the Massachusetts Institute of Technology, is a general framework for solving discrete finite-element approximations to advection-diffusion-reaction type partial differential equations, such as scalar advection-diffusion, Navier-Stokes, and RANS equations. A range of finite-element methods are currently implemented in SANS, including high-order discontinuous, hybridized discontinuous, and continuous Galerkin finite-element methods. The variational multiscale method with discontinuous subscales [30, 31] discretization is used to compute all solutions to the RANS equations presented here. Boundary conditions are weakly enforced, and forces are computed using the residual balance at the boundary.

The nonlinear system of equations is solved using pseudotime continuation (PTC) damped Newton's method with a line search to ensure that residuals decrease. The complete linearization of the residual is computed via operator overloaded automatic differentiation [32]. The PTC algorithm computes an element local time step based on the characteristic speed, element size, and a Courant-Friedrichs-Lewy (CFL) number. The inverse CFL is driven toward zero such that a Newton-like convergence rate is recovered. The portable, extensible toolkit for scientific computation framework [33-35] is used to solve the linear system for each PTC iteration with restarted generalized minimal residual (GMRES) [36] preconditioned with a Direct Lower Upper (Direct-LU) factorization. Parallel computations use the restricted additive Schwarz preconditioner with three layers of overlap. The Direct-LU preconditioner is applied to each subdomain, and restarted GMRES is applied to the global system. Adjoint systems are solved using the same linear solver as the primal. All discrete solutions are converged to near machine-zero residuals.

IV. Test Case 1: Joukowski Airfoil

This 2D test case is designed as a relatively simple verification case for implementation of the SA-neg-QCR2000-R RANS equations where theoretically optimal convergence rates for drag coefficients can be observed. For adjoint-consistent discretization methods of nominal order $(P+1)$, the optimal convergence rate of the error in the drag coefficient is expected to be $2P$. Without adjoint consistency, the drag error convergence rate is expected to be at least $P+1$.

The Joukowski airfoil chosen for this test (Fig. 1) is a symmetric aerodynamic analytical shape that features a cusped trailing edge. A solution for a high-Reynolds-number flow at zero degrees angle of attack is expected to be smooth; although, there is a skin-friction singularity at the trailing edge. The flow conditions for this test case are the following: the freestream Mach number is $M_\infty = 0.15$, the Reynolds number is $Re_c = 6 \times 10^6$ based on the airfoil chord, the angle of attack is $\alpha = 0°$, and the reference temperature is $T_{ref} = 520$ °R. A no-slip adiabatic-wall boundary condition is set at the airfoil, and the far-field boundary conditions are based on an inviscid characteristic method.

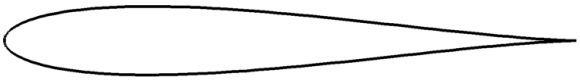

Fig. 1 Joukowski airfoil.

The family of fixed grids used in this study includes six nested, quadrilateral grids that follow the classic meshing guidelines requiring grid lines to be near orthogonal to the geometry and the sizes of neighboring elements to be similar. The grids are referenced as Grid 0 to Grid 5. The Joukowski conformal map is used to generate grids with nearly orthogonal grid lines. The coarsest Grid 0 is composed of 48×16 quadrilateral cells (48×17 grid nodes), the finest Grid 5 grid is composed of 1536×512 quadrilateral cells (1536×513 grid nodes). Three views of Grid 2 are shown in Fig. 2. The computational domain extends 100 chord lengths from the airfoil. The grids are stretched toward the viscous surface, toward the x-axis ($y = 0$) upstream and downstream of the airfoil, and toward the grid line that goes through the trailing edge and is orthogonal to the x-axis at the trailing edge. The wake grid opens as the mesh progresses aft of the airfoil trailing edge to reduce the maximum cell aspect ratio to approximately 100 near the outflow boundary. The grid clustering at the leading edge serves to capture the weak stagnation pressure singularity. The grid clustering at the trailing edge is needed to capture the skin-friction singularity. The grid spacing

near the leading and trailing edges was repeatedly adjusted to produce grids that facilitate observation of expected error rates in the drag output with grid refinement. These geometry and grids have been used for verification of SA-neg-QCR2000 model [39].

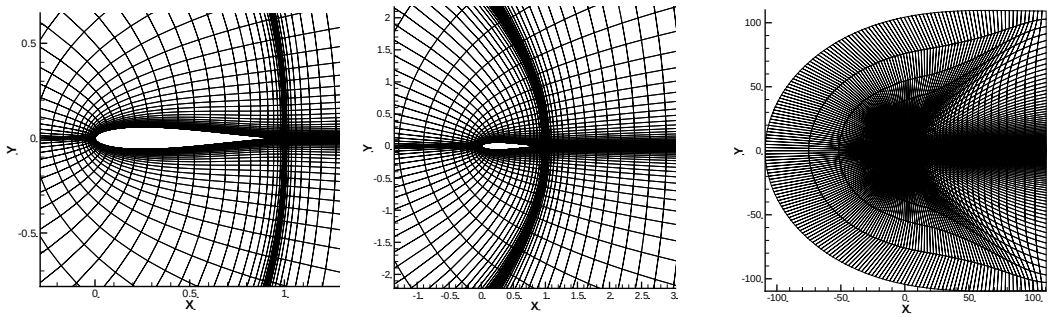

(a) Near surface view (b) Wake view (c) Global view

Fig. 2 Grid 2 for Joukowski airfoil.

FUN3D solutions are computed on six fixed quadrilateral grids, Grid 0 through Grid 5, and provide nominal second-order accuracy, although a first-order approximation to the convection term of the turbulence model is used. The specific implementation is based on 3D one-cell-wide hexahedral grids. The FUN3D formulation is not adjoint consistent. SANS computes solutions on five fixed grids, Grids 0 through Grid 4, and on adapted grids generated by Mesh Optimization via Error Sampling and Synthesis (MOESS) tool [37, 38]. The grid adaptation process is governed by the adjoint-based error estimator targeting reduction of the error in the drag coefficient. SANS solutions on the fixed grids are computed on truly 2D grids, in which each quadrilateral cell is divided into two triangular cells; the number of grid nodes remain unchanged. SANS solutions use polynomials of degrees $P = 1, 2,$ and 3, and provide nominal second-, third-, and fourth-order accuracy, respectively. The SANS formulation is adjoint consistent. All solutions reported in this section have the root mean square (rms) norm of the meanflow and turbulence-model residuals converged below 10^{-13}.

The aerodynamic coefficients are computed using the freestream Mach number of 0.15. Table 1 collects grid convergence results for the total-drag (C_D), pressure-drag $\left(C_{Dp}\right)$, and viscous-drag (C_{Dv}) coefficients computed with the SA-neg-QCR2000-R model with $C_{rot} = 1.0$. Note that $C_D = C_{Dp} + C_{Dv}$. The nominal grid spacing is computed as $h = N^{-1/2}$, where N are the degrees of freedom (DOF). For FUN3D and SANS-P1 solutions, DOF are 2D grid points. Higher-order SANS solutions have more DOF on the same grids reflecting the increased operation count in computing higher-order residuals. The effect of the rotation correction on the solutions is minor; all drag coefficients are close to the corresponding coefficients computed with the SA-neg-QCR2000 model [39] for the same geometry, grids, and flow conditions.

For the error estimate, the "truth" values for the coefficients of total drag, pressure drag, and viscous drag are taken as the corresponding coefficients computed from the SANS-P3 solution on the finest adapted grid. The error in a coefficient is estimated as the magnitude (absolute value) of the difference between the coefficient computed on a given grid and the "truth" value of the coefficient. Note that the uncertainty in the truth values is on the order of 10^{-6}; thus, all estimates of errors that are comparable or smaller than the uncertainty threshold are not reliable. Nevertheless, estimated errors are plotted below for all solutions for completeness.

Figure 3 shows convergence of the total-drag coefficient (Fig. 3(a)) and the error in the total-drag coefficient (Fig. 3(b)). The slopes that represent convergence of second, fourth, and sixth orders are also shown in Fig. 3(b). Convergence of the total-drag coefficient shown in Fig. 3(a) is mostly regular and monotonic for all solutions that have errors significantly greater than 10^{-6}. The SANS-P1 total drag coefficients computed on the fixed grids converge to the truth value from above but cross the truth value on Grid 4. In Fig. 3(b), FUN3D shows a convergence rate close to the optimal second-order rate, as expected. The SANS-P1 convergence rate apparently exceeds the optimal second-order rate on adapted and fixed grids. The SANS-P1, SANS-P2, and SANS-P3 convergence rates are similar on coarser fixed grids

and close to the fourth-order rate, which is the optimal rate for P2 solutions. The SANS-P2 and SANS-P3 convergence rates on adapted grids are not regular but the corresponding total drag coefficients exhibit significantly smaller errors per DOF than the coefficients computed on the fixed grids.

Table 1 Joukowski airfoil: convergence of drag coefficients on fixed grids.

Solution	Grid	N	$h = N^{-1/2}$	C_D	C_{Dp}	C_{Dv}
FUN3D	Grid 0	816	0.035007	0.061721	0.051628	0.010093
	Grid 1	3,168	0.017767	0.021942	0.014936	0.007006
	Grid 2	12,480	0.008951	0.010441	0.003818	0.006623
	Grid 3	49,536	0.004493	0.008284	0.001656	0.006627
	Grid 4	197,376	0.002251	0.007947	0.001310	0.006638
	Grid 5	787,968	0.001127	0.007891	0.001256	0.006635
SANS-P1	Grid 0	816	0.035007	0.051355	0.038668	0.013797
	Grid 1	3,168	0.017767	0.013792	0.006470	0.007342
	Grid 2	12,480	0.008951	0.008581	0.002008	0.006572
	Grid 3	49,536	0.004493	0.007925	0.001382	0.006543
	Grid 4	197,376	0.002251	0.007868	0.001280	0.006588
SANS-P2	Grid 0	3,168	0.017767	0.008873	0.002026	0.006850
	Grid 1	12,480	0.008951	0.007916	0.001277	0.006642
	Grid 2	49,536	0.004493	0.007874	0.001244	0.006630
	Grid 3	197,376	0.002251	0.007873	0.001244	0.006629
	Grid 4	787,968	0.001127	0.007873	0.001245	0.006629
SANS-P3	Grid 0	7,056	0.011905	0.007910	0.001263	0.006655
	Grid 1	27,936	0.005983	0.007874	0.001243	0.006631
	Grid 2	111,168	0.002999	0.007873	0.001245	0.006629

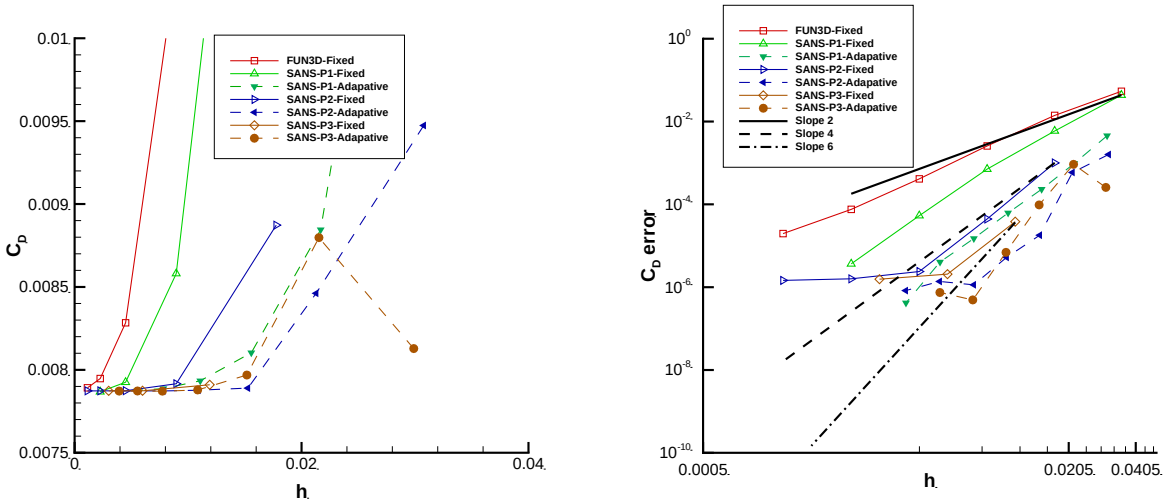

(a) Total drag (b) Error in total drag

Fig. 3 Joukowski airfoil: grid convergence of total-drag coefficient, $C_{D,truth} = 0.007872$.

Convergence plots of pressure-drag coefficients and the corresponding errors are shown in Fig. 4. The FUN3D and all SANS C_{Dp} coefficients on the fixed grids and the SANS-P1 coefficients on the adapted grids converge monotonically. The SANS-P2 and SANS-P3 coefficients oscillate around the truth value on the fine adapted grids. The convergence rate of the FUN3D C_{Dp} coefficient is higher than the optimal second-order rate. The SANS-P1 C_{Dp} coefficients converge with the optimal second-order rate on the fixed and adapted grids; the coefficients on the adapted grids show much higher accuracy per DOF. The SANS-P2 convergence rate is super-optimal on the coarse fixed grids before the error approaches the truth-

uncertainty threshold, the SANS-P3 convergence rate on the fixed grids is less than optimal. The SANS-P2 and SANS-P3 coefficients on adapted grids converge less regularly but exhibit higher accuracy per DOF.

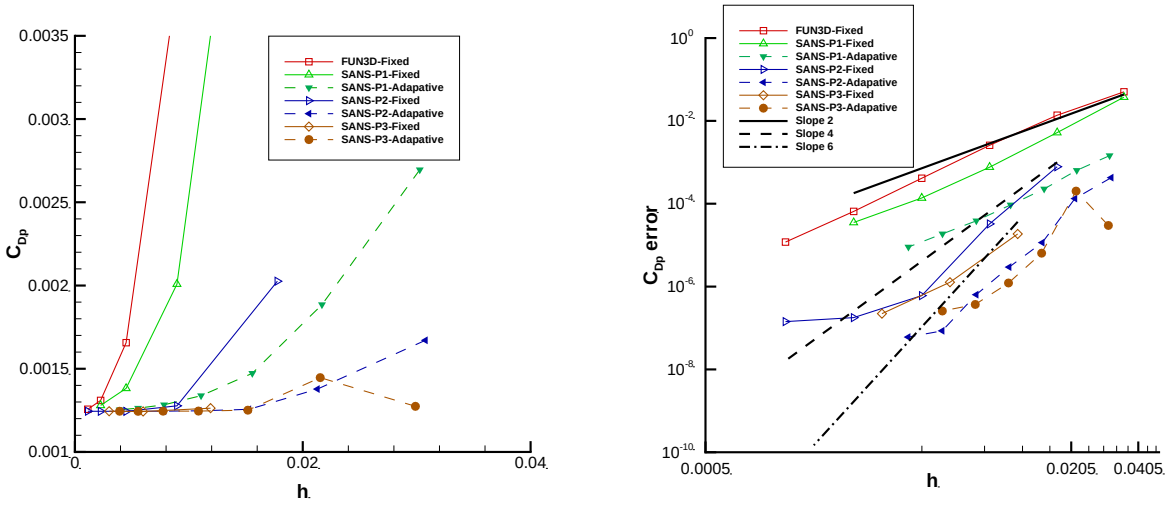

(a) Pressure drag (b) Error in pressure drag

Fig. 4 Joukowski airfoil: grid convergence of pressure drag coefficient, $C_{Dp,truth} = 0.001244$.

Convergence plots of viscous-drag coefficients and the corresponding errors are shown in Fig. 5. Convergence of FUN3D and SANS-P1 C_{Dv} coefficients is highly erratic and nonmonotonic, but, on average, the convergence rates are close to the optimal second-order rate. The SANS-P2 and SANS-P3 coefficients converge monotonically on the fixed grids and show very similar convergence rates that are close to the fourth-order rate before the errors approach the uncertainty threshold. Similar to other drag coefficients, the SANS-P2 and SANS-P3 C_{Dv} coefficients on adapted grids converge less regularly but exhibit higher accuracy per DOF.

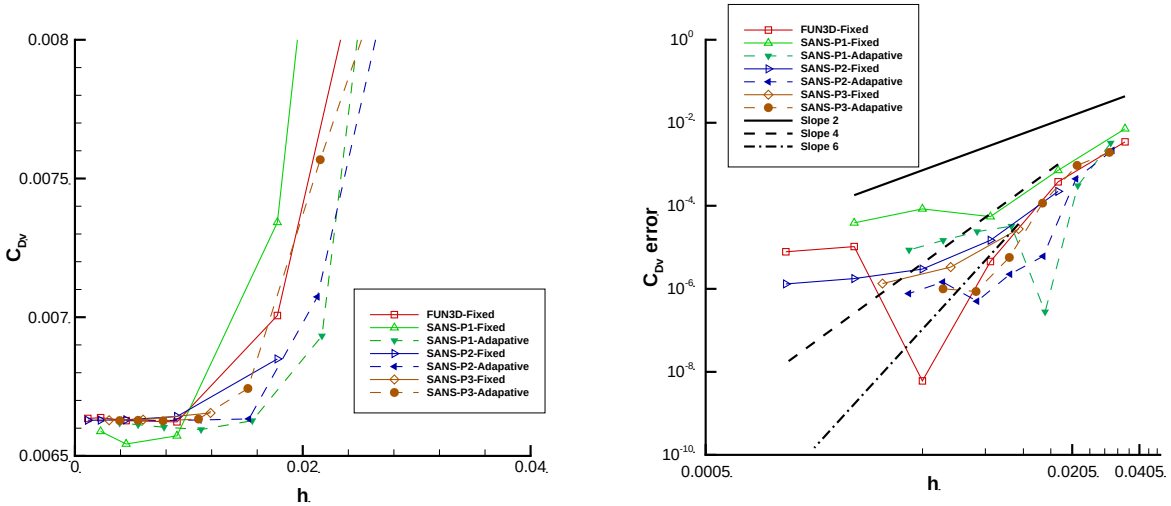

(a) Viscous drag (b) Error in viscous drag

Fig. 5 Joukowski airfoil: grid convergence of viscous drag coefficient, $C_{Dv,truth} = 0.006627$.

V. Test Case 2: Extruded NACA 0012 Wing in Tunnel

A. Geometry, Flow, and Boundary Conditions

The test case considers a separated subsonic flow around a 3D configuration that represents an NACA 0012 wing extruded from a wall of a tunnel with a rectangular cross-section. The model is similar to the one considered in Ref. [8]. The rectangular wing has a span of 0.75 and a constant cross-section in the shape of the NACA 0012 airfoil with a sharp trailing edge and unit chord. The wing has a rounded tip. The tunnel test section has unit width, height of $\frac{2}{3}$, and length of 3. The wing is mounted on the test-section wall corresponding to $y = 0$ with pitch angle of 10 degrees; the opposite wall is located at $y = -1$. The quarter-chord location of the root airfoil corresponds to $x = 0$. The limits of the x- and z-coordinates of the tunnel test section are $-1 \leq x \leq 2$ and $-\frac{1}{3} \leq z \leq \frac{1}{3}$, respectively. Comparing to Ref. [8], the x range has been increased.

The inflow conditions are Mach number of 0.2, Reynolds number of 4.6×10^6 based on the unit length, and an angle of attack of 0 degrees with respect to the tunnel. The reference temperature is $T_{ref} = 521$ °R. No-slip wall boundary conditions are assigned to the wing surface and the test section of the tunnel. Upstream and downstream of the test section, extensions with tangency-wall (perfect slip) boundary conditions are added. The upstream extension, $-2 \leq x < -1$, has the same rectangular cross-section as the test section. For meanflow, subsonic inflow boundary conditions are specified at $x = -2$, where the ratio of the total pressure to the reference pressure is set to 1.02828 (based on the Mach number of 0.2), the ratio of the total temperature to the reference temperature is set to 1.008, the flow angle is set to zero, and the velocity magnitude is extrapolated from the interior. The downstream tangency-wall extension section narrows over $2 < x \leq 6.5$ to a rectangular cross-section of width 0.9 and height 0.6 centered at $z = 0$. This converging section is needed to increase the flow speed and prevent reversed flow at the outflow boundary at $x = 6.5$, where the ratio of the back pressure to the reference pressure is set to 1.0 and all other solution quantities are extrapolated from the interior. The distance function used in the turbulence model is computed from the closest wall, either no-slip wall or tangency wall. The turbulence variable is set to zero on all walls, to the freestream ratio at the inflow boundary, and extrapolated from the interior at the outflow boundary. Figure 6 shows a global view of the computational geometry and a view of the wing inside the tunnel test section. The blue and grey colors indicate no-slip and tangency wall boundaries, respectively; the red and green colors indicate the inflow and outflow boundaries, respectively.

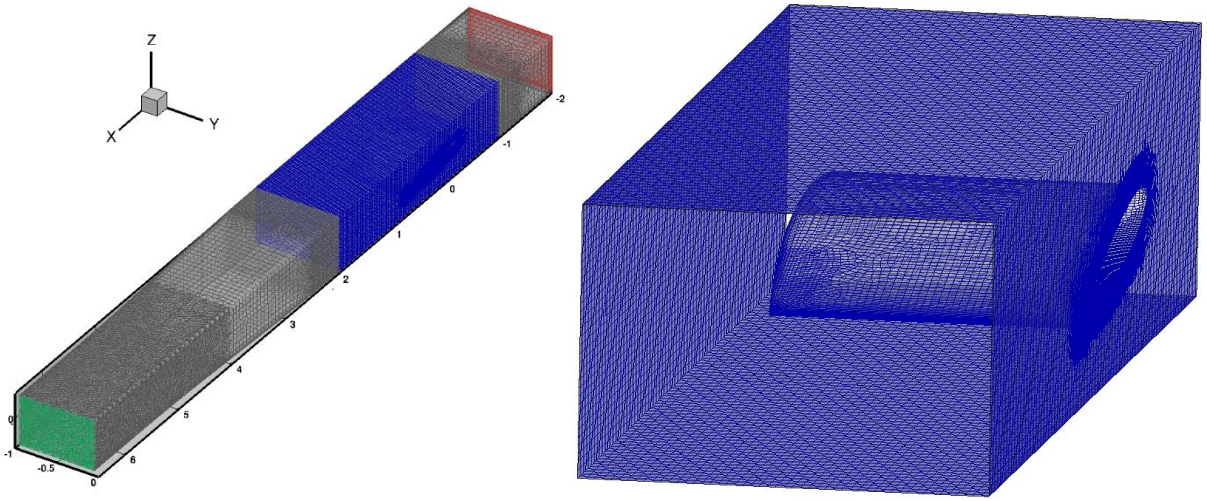

(a) Global view of geometry (b) Wing in test section

Fig. 6 Extruded NACA 0012 wing: surface grids.

Figure 7 shows the solution Q-criterion isosurface colored by the vorticity magnitude contours. A strong tip vortex and geometrical features associated with corners and interfaces between surfaces with different boundary conditions are highlighted.

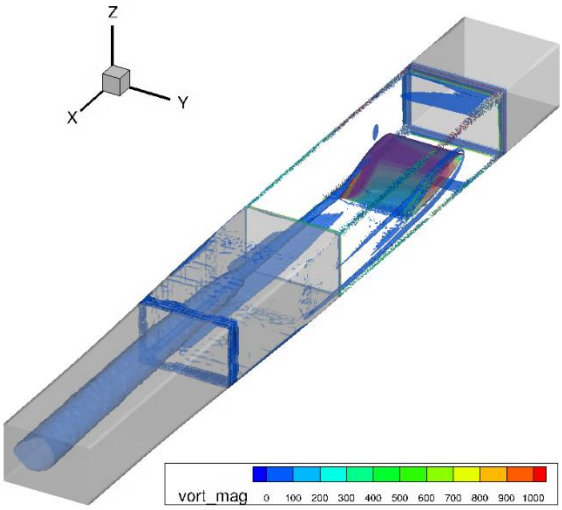

Fig. 7 Extruded NACA 0012 wing: vorticity contours.

B. Grids

A family of nine unstructured grids has been generated by Cadence® software Pointwise† and uses Glyph script package GeomToMesh [40]. The grids are generated by a consistent coarsening/refinement of the baseline grid that is tagged as Grid 1.0. The grid tag indicates the intended scaling factor of the grid edges. For example, the edges of Grid 0.5 are intended to be two times longer and the edges of Grid 2.0 are intended to be two times shorter than the edges of the baseline Grid 1.0. The Pointwise grids are referred to as fixed grids to distinguish from the adapted grids that are also used in the study. The grid generation process strictly follows the best practices in generation of grid families that provide user-specified resolution of all geometrical features and maintain smoothness of the surface and volume grids. The coarsest Grid 0.5 has 2.6 million grid points; the finest Grid 2.5 has 90 million grid points. Table 4 shows grid statistics.

Table 4 Extruded NACA 0012 wing: statistics of fixed grids.

Grid tag	Tetrahedra	Prisms	Pyramids	Hexahedra	Points
0.50	1,621,703	66,678	89,813	2,263,869	2,618,268
0.75	5,783,545	102,108	161,541	4,812,270	5,907,447
1.00	14,405,654	137,367	253,387	8,317,833	10,891,035
1.25	29,147,202	175,130	366,488	12,684,582	17,741,411
1.50	51,271,350	218,680	503,967	17,912,051	26,667,090
1.75	82,717,090	271,014	666,375	24,252,915	38,234,981
2.00	125,170,334	326,234	841,549	31,460,819	52,458,483
2.25	180,254,204	363,357	1,039,284	39,541,502	69,604,505
2.50	250,206,779	417,605	1,256,432	48,478,126	90,023,530

C. Solutions

FUN3D solutions are computed on all nine fixed grids. Note the importance of high precision in representation of the ratio of the total pressure to the reference pressure (1.02828) and the ratio of the total

† http://www.pointwise.com, accessed 11/21/2022

temperature to the reference temperature (1.008). Rounding the ratios to fewer significant digits (1.03 and 1.01, respectively) resulted in drag variation on the order of several dozens of counts. SANS computes P=1 solutions on adapted grids generated by MOESS. All solutions reported in this section have the rms norm of the meanflow and turbulence-model residuals converged below 10^{-10}, which is the machine-zero level on the fine fixed grids. The aerodynamic coefficients are computed using reference area of 0.75 and Mach number of 0.2. Grid convergence of the lift and drag coefficients is shown in Fig. 8. The characteristic mesh size is computed as $\mathrm{h} = N^{-1/3}$, where N is the number of grid points. The aerodynamic coefficients are integrated over all no-slip walls, including the surfaces of the tunnel test section.

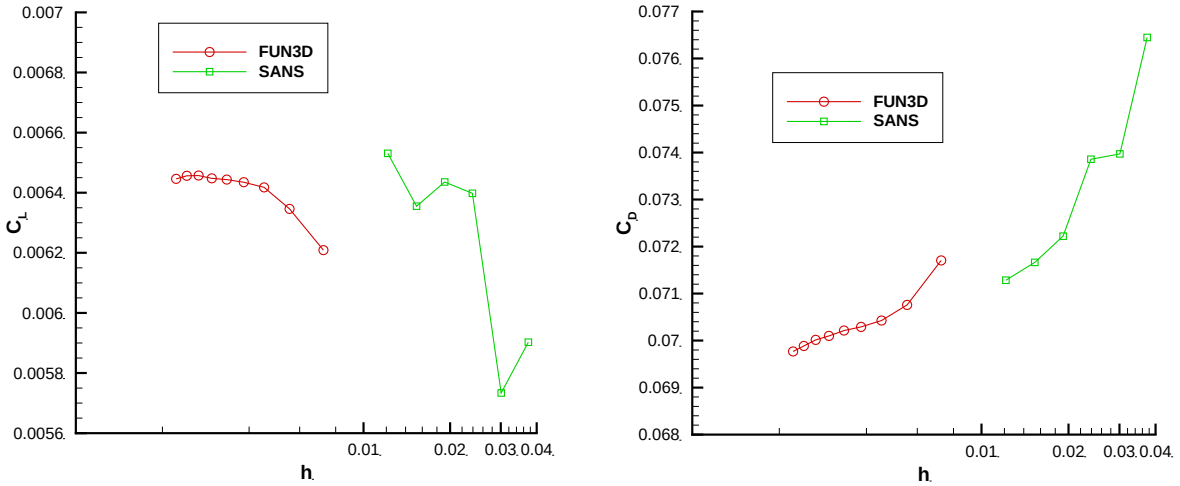

(a) Lift (b) Drag

Fig. 8 Extruded NACA 0012 wing: grid convergence of aerodynamic coefficients.

Both lift and drag coefficients are converging but have not grid converged yet. Although the lift coefficients computed by FUN3D on the currently finest fixed grid and by SANS on the currently finest adapted grid differ by less than 1.5%, the coefficients have not settled and show a visible variation with grid refinement. The grid convergence of the lift coefficient is not monotonic. The drag coefficients converge monotonically but also have not settled. The drag coefficients computed by FUN3D and SANS appear heading to a similar limit with grid refinement. The difference between FUN3D and SANS coefficients computed on the currently finest grids is about 14 counts. Finer grids are needed to confidently establish the lift and drag coefficients.

VI. Test Case 3: Simplified High-Lift Wing-Body Common Research Model

A. Geometry, Flow, and Boundary Conditions

The test case considers a semispan high-lift configuration that is designated as CRM-HL-WB. CRM-HL-WB is the simplest configuration in the family of standard high-lift geometries designed for studying aerodynamic phenomena associated with high-lift flow regimes. The original NASA high-lift common research model (CRM-HL) [41] is a representative high-lift configuration used in the 4th High-Lift Prediction Workshop (HLPW) [42]. The CRM-HL model is a complex configuration that features fuselage, wing, nacelle, pylon, leading-edge slats with under-slat wings, trailing-edge flaps, horizontal tail, main landing gear, and aileron. The CRM-HL-WB model considered here is a simplified version of CRM-HL that is designed for verification of solvers participating in HLPW. The CRM-HL-WB model has similar fuselage and high-lift wing geometries as the CRM-HL model but it is stripped of all other geometric features. The model has wing semispan of 1156.75 in. The wing has a thin blunt trailing edge and a rounded tip cap. The mean aerodynamic chord (MAC) is 275.8 in. The reference area is 297,360.0 in^2. The entire

computational domain is a rectangular cuboid with dimensions $-65{,}000 \leq x \leq 65{,}000;\ 0 \leq y \leq 65{,}000;$ $-65{,}000 \leq z \leq 65{,}000$. The computational domain and the wing-body geometry are illustrated in Fig. 9.

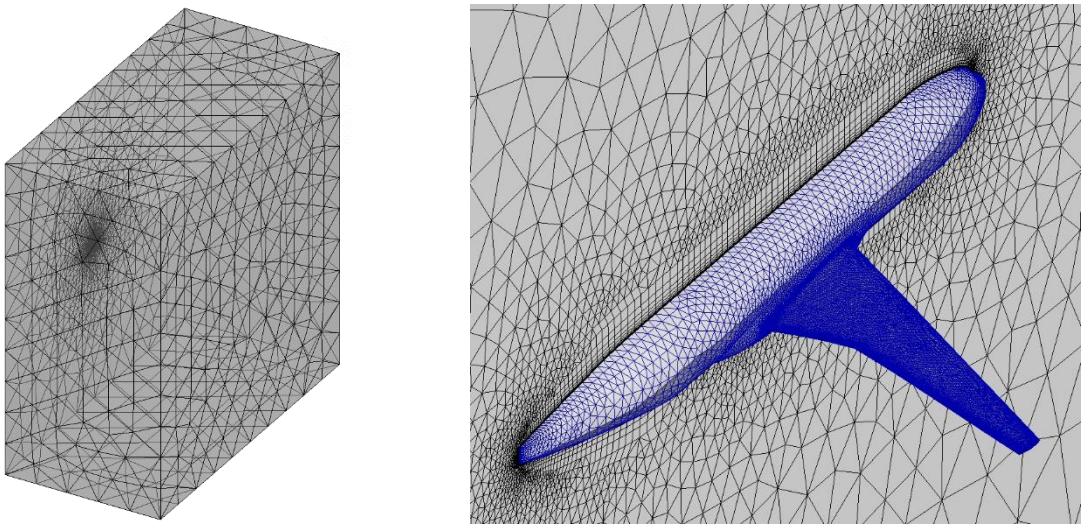

(a) Global view of computational grid (b) Surface grid and symmetry plane

Fig. 9 CRM-HL-WB: grid convergence of aerodynamic coefficients.

The freestream flow conditions are Mach number of 0.2, Reynolds number of 5.6×10^6 based on the MAC, and an angle of attack of 11 degrees. The reference temperature is $T_{ref} = 521$ °R. The no-slip boundary condition is assigned to the wing and fuselage surface. Symmetry is specified at the $y = 0$ plane. The farfield boundary conditions based on Riemann invariants are assigned at all other boundaries of the computational domain. For the current verification studies, the target characteristics are grid convergence of lift and drag coefficients.

B. Grids

A family of seven unstructured mixed-element grids has been generated by experts using the Pointwise Glyph script package GeomToMesh [40] and the best grid-generation practices. The grids are parametrized by the number of surface elements placed across the thin blunt trailing edge of the wing; this number is reflected in the grid tag. The coarsest grid, Grid 1v, has a single element across the trailing edge. Finer grids place multiple elements across the trailing edge, and all grid elements are scaled accordingly. Table 5 shows the grid statistics. The grids are referred to as fixed grids to distinguish them from the adapted grids that will be used later. Figure 9 shows the coarsest Grid 1v.

Table 5 CRM-HL-WB: statistics of fixed grids.

Grid tag	Tetrahedra	Prisms	Pyramids	Points
1v	1,050,501	1,509,398	21,289	956,070
3v	3,522,591	9,209,000	72,125	5,275,061
5v	8,103,392	27,858,957	126,162	15,439,756
7v	15,483,899	62,266,147	233,318	33,980,621
9v	26,206,961	117,276,602	382,315	63,404,323
11v	41,131,004	198,147,783	569,730	106,478,104

C. Solutions

Only FUN3D solutions have been computed on the fixed grids. Solutions computed on grids 1v to 7v have the rms norm of the meanflow and turbulence-model residuals converged below 10^{-9}; the solutions computed on grid 9v and 11v converged to the rms residual norm of 10^{-8}, which is close to the machine zero on these grids. The surface pressure contours of the solution computed on Grid 7v are shown in Fig.

10. The aerodynamic coefficients are computed using the freestream Mach number of 0.2. Grid convergence of the lift and drag coefficients is shown in Fig. 11. The characteristic mesh size is computed as $h = N^{-1/3}$. Both the aerodynamic coefficients appear to converge with grid refinement, but have not converged yet. Finer grids are needed to observe grid converged aerodynamic coefficients.

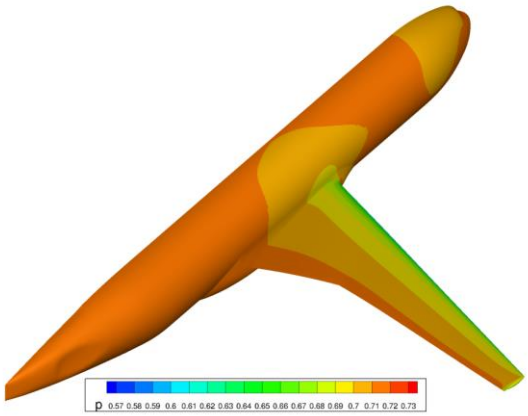

Fig. 10 CRM-HL-WB: surface pressure contours.

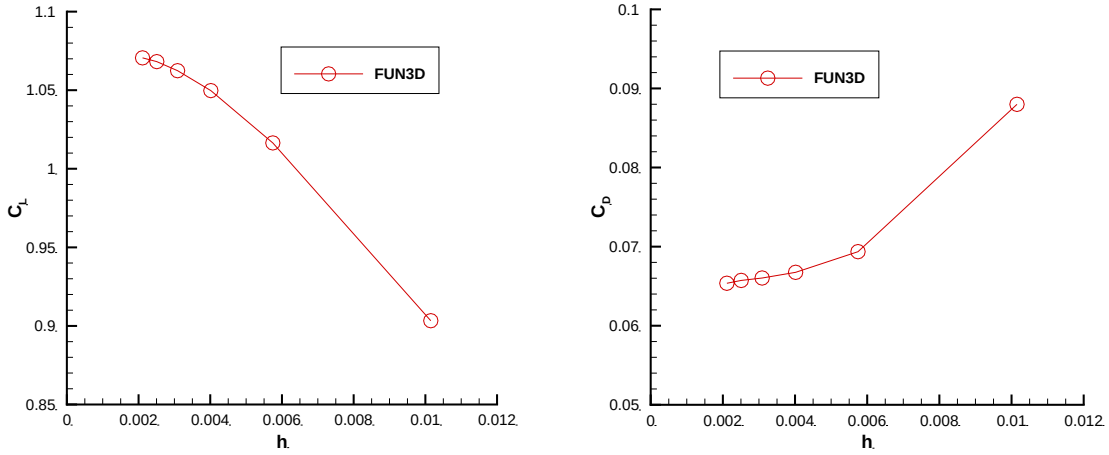

(a) Lift (b) Drag

Fig. 11 CRM-HL-WB: grid convergence of aerodynamic coefficients.

VII. Concluding Remarks

In preparation for High-Fidelity Computational Fluid Dynamics (CFD) Verification Workshop (HFCFDVW), three test cases are presented for a suite of verification cases for Reynolds-averaged Navier-Stokes (RANS) solvers with a nonlinear Spalart-Allmaras (SA-[neg]-QCR2000-R) turbulence model. This model accounts for anisotropy of turbulence stresses and can predict secondary recirculation in turbulent corner flows. This recirculation cannot be captured with linear eddy-viscosity models based on the Boussinesq assumption. The simple rotation correction (designated as –R) is used to mitigate generation of spurious eddy viscosity within vortices. A weak rotation correction corresponding to $C_{rot} = 1.0$ is chosen for the mandatory verification campaign. A more aggressive correction corresponding to $C_{rot} = 2.0$ is

suggested as an option. The formulation that is compatible with the SA-neg version of the turbulence model has been presented in detail. The SA-neg extension is often essential for achieving converged solutions on complex grids.

The verification test cases include (1) a subsonic two-dimensional (2D) flow around a Joukowski airfoil, (2) a three-dimensional (3D) subsonic separated flow around an extruded NACA 0012 wing in a tunnel, and (3) a 3D subsonic separated flow around a Boeing high-lift common research model (CRM) that is intended for verification of solvers participating in the high-lift prediction workshop. Two well-established RANS solvers have been used to provide solutions for these test cases: FUN3D is a NASA unstructured-grid node-centered finite-volume solver and SANS is a high-order finite-element solver developed at the Massachusetts Institute of Technology. All solutions are computed for $C_{rot} = 1.0$.

The Joukowski-airfoil test case is a simple verification case designed to demonstrate the optimal convergence rate for high-order solvers with and without adjoint-consistent discretizations. A family of uniformly-refined nested quadrilateral grids has been generated for the study. The finest grid in the family includes more than 3 million grid nodes. Seven different types of solutions have been computed. FUN3D solutions computed on the expert generated fixed grids are nominally second-order accurate. SANS has provided three adjoint-consistent discretizations based on polynomials of degree $P = 1, 2, \text{and } 3$. The optimal convergence rate for adjoint-consistent discretizations is 2P. The SANS solutions have been computed on the fixed grids and on adapted grids governed by the adjoint-based estimator of the error in the total drag coefficient.

An internal flow around an extruded NACA 0012 wing mounted on a tunnel wall is chosen as a medium complexity verification case. This case features a simple wing in a tunnel that produces a tip vortex. A similar geometry was used in the original paper that introduced the –R correction. A family of nine fixed unstructured grids has been generated by experts for this study. The grid complexity ranges from 2 million grid points to 90 million grid points. FUN3D has computed solutions on the fixed grids. SANS-P1 solutions have been computed on adapted grids. All solutions converged to machine zero residuals. Lift and drag coefficients computed by the two codes are close to each other on the corresponding finest grids, but the grid converged values of the aerodynamic coefficients have not been established yet. Finer grids are needed to compute lift and drag with a better accuracy. This verification exercise has helped to establish sensitivity of the drag coefficient to the precision of the total pressure and total temperature used in the formulation of the inflow boundary conditions.

An external flow around a wing-body common research model (CRM-HL-WB) that is closely related to the high-lift common research model (CRM-HL) used in the 4th High-Lift Prediction Workshop represents a challenging verification case. CRM-HL-WB was designed by Boeing for verification of solvers participating in future high-left prediction workshops. Seven grids have been generated by experts for this case. The coarsest grid includes 956 thousand grid points; the finest grid includes 106 million grid points. FUN3D solutions have been computed on the fixed grids. The lift and drag coefficients computed from these solutions approach but have not achieved grid convergence. Finer grids and solutions computed by other solvers are needed to confidently establish grid converged values of the aerodynamic coefficients.

The presented test cases have been suggested to facilitate organization of a working group that will include prospective HFCFDVW participants interested in verification of their RANS solvers. The group will work during the next year to develop best practices for verification of practical RANS solvers. The final recommendations will be reported at the HFCFDVW sessions and disseminated in subsequent publications.

Acknowledgments

The Transformative Tools and Technologies (TTT) project of the Transformative Aeronautics Concepts Program (TACP) and Commercial Supersonic Technology (CST) projects of Advanced Air Vehicles Program (AAVP) partially funded the work reported herein. The first two authors were supported by the NASA Langley Research Center (LaRC) under cooperative agreement 80LARC17C0004 with the National Institute of Aerospace (NIA). The third author was supported by the Boeing Corporation with Dr. Andrew

Cary as technical monitor. Most of computations were performed on the NASA LaRC K-Cluster. The authors are grateful to Steve Karman (Oak Ridge National Laboratory) and Nick Wyman (Cadence) for generating grids for the CRM-HL-WB and NACA-0012 configurations, and to Adam Clark (Boeing) for information about the CRM-HL-WB configuration.

References

[1] "High Fidelity CFD Workshop 2022," retrieved 22 November 2022. https://turbmodels.larc.nasa.gov/highfidelitycfd_workshop2022.html

[2] "5th International Workshop on High-Order CFD Methods," retrieved 22 November 2022. https://how5.cenaero.be

[3] "4th International Workshop on High-Order CFD Methods," retrieved 22 November 2022. https://how4.cenaero.be/

[4] Diskin, B., Anderson, W. K., Pandya, M. J., Rumsey, C. L., Thomas, J. L., Lui, Y., and Nishikawa, H., "Grid Convergence of Three-Dimensional Benchmark Turbulent Flows," AIAA 2018-1102, 2018. https://doi.org/10.2514/6.2018-1102

[5] Diskin, B. and Thomas, J. L., "Introduction: Evaluation of RANS Solvers on Benchmark Aerodynamic Flows," *AIAA Journal*, Vol. 54, No. 9, 2016, pp. 2561-2562. https://doi.org/10.2514/1.J054642

[6] Spalart, P. R. and Allmaras, S. R., "A One-Equation Turbulence Model for Aerodynamic Flows," *Recherche Aerospatiale*, No. 1, 1994, pp. 5-21. https://turbmodels.larc.nasa.gov/Papers/RechAerosp_1994_SpalartAllmaras.pdf

[7] Spalart, P. R., "Strategies for Turbulence Modelling and Simulation," *International Journal of Heat and Fluid Flow*, Vol. 21(3), 2000, pp. 252-263. https://doi.org/10.1016/S0142-727X(00)00007-2

[8] Dacles-Mariani, J., Zilliac, G. G., Chow, J. S., and Bradshaw, P., "Numerical/Experimental Study of a Wingtip Vortex in the Near Field," *AIAA Journal*, Vol. 33(9), 1995, pp. 1561-1568. https://doi.org/10.2514/3.12826

[9] Dacles-Mariani, J., Kwak, D., and Zilliac, G. G., "On Numerical Errors and Turbulence Modeling in Tip Vortex Flow Prediction," *Int. J. for Numerical Methods in Fluids*, Vol. 30(1), 1999, pp. 65-82. https://doi.org/10.1002/(SICI)1097-0363(19990515)30:1<65::AID-FLD839>3.0.CO;2-Y

[10] Allmaras, S. R., Johnson, F. T., and Spalart, P. R., "Modifications and Clarifications for the Implementation of the Spalart-Allmaras Turbulence Model," ICCFD7-1902, Seventh International Conference on Computational Fluid Dynamics (ICCFD7), Big Island, Hawaii, 2012. https://www.iccfd.org/iccfd7/assets/pdf/papers/ICCFD7-1902_paper.pdf

[11] "NASA Turbulence Modeling Resource," retrieved 22 November 2022. https://turbmodels.larc.nasa.gov/

[12] HFCFDVW website, retrieved 29 November 2022. https://github.com/HighFidelityCFDVerificationWorkshop

[13] Tannehill, J. C., Anderson, D. A., and Pletcher, R. H., "Computational Fluid Mechanics and Heat Transfer," third edition, Taylor & Francis, 2012, Chap. 5.

[14] White, F. M., "Viscous Fluid Flow," McGraw Hill, New York, 1974, p. 28.

[15] Murayama, M., Ito, Y., Furuya, R., and Tanaka, K., "JAXA's Results of Fixed Grid RANS Simulations for the Fourth High Lift Prediction Workshop," AIAA 2022-3743. https://doi.org/10.2514/6.2022-3743

[16] Biedron R. T., Carlson J. R., Derlaga J. M., Gnoffo P. A., Hammond D. P., Jones W. T., Kleb B., Lee-Rausch E. M., Nielsen E. J., Park M. A., Rumsey C. L., Thomas J. L., Thompson K. B., Walden, A. C., Wang, L., and Wood W. A., "FUN3D Manual: 13.7," NASA TM 2020-5010139, 2020.

[17] Nielsen, E. J., and Diskin, B., "High-Performance Aerodynamic Computations for Aerospace Applications," *Parallel Computing*, Vol. 64, 2017, pp. 20–32. https://doi.org/10.1016/j.parco.2017.02.004

[18] Walden, A., Nielsen, E. J., Zubair, M., Linford, J. C., Wohlbier, J. G., Luitjens, J. P., Orender, J., Beekman, I., Khuvis, S., and Shende, S. S., "Unstructured-Grid CFD Algorithms on Many-Core Architectures," Technical Research Posters of International Supercomputing Conference for High Performance Computing, Networking, Storage, and Analysis. p. 17, 2017. https://sc17.supercomputing.org/SC17%20Archive/tech_poster/poster_files/post134s2-file3.pdf
[19] Walden, A., Nielsen, E. J., Diskin, B., and Zubair, M., "A Mixed Precision Multicolor Point-Implicit Solver for Unstructured Grids on GPUs," 2019 IEEE/ACM 9th Workshop on Irregular Applications: Architectures and Algorithms (IA3), Denver, CO, USA, 2019, pp. 23-30. https://doi.org/10.1109/IA349570.2019.00010
[20] Nastac G., Walden A., Nielsen E. J., and Frendi K., "Implicit Thermochemical Nonequilibrium Flow Simulations on Unstructured Grids using GPUs," AIAA 2021-0159, 2021. https://doi.org/10.2514/6.2021-0159
[21] Walden A., Nielsen E. J., Korzum A., et al., "Landing on Mars: Petascale Unstructured Grid Computational Fluid Dynamics on Summit," International Workshop on OpenPOWER for HPC, ISC, 2019. https://indico-jsc.fz-juelich.de/event/87/material/slides/8.pdf
[22] Roe P. L., "Approximate Riemann Solvers, Parameter Vectors, and Difference Schemes," Journal of Computational Physics, Vol. 43, No. 2, 1981, pp. 357–372. https://doi.org/10.1016/0021-9991(81)90128-5.
[23] Burg C. O. E., "Higher Order Variable Extrapolation for Unstructured Finite Volume RANS Flow Solvers," AIAA 2005–4999, 2005. https://doi.org/10.2514/6.2005-4999
[24] van Leer B., "Towards the Ultimate Conservative Difference Scheme, V. A Second Order Sequel to Godunov's Method," Journal of Computational Physics, Vol. 32, No. 1, 1979, pp. 101–136. https://doi.org/10.1016/0021-9991(79)90145-1
[25] Barth T. J., "Numerical Aspects of Computing Viscous High Reynolds Number Flows on Unstructured Meshes," AIAA 91–0721, 1991. https://doi.org/10.2514/6.1991-721
[26] Haselbacher A. C., A Grid-Transparent Numerical Method for Compressible Viscous Flow on Mixed Unstructured Meshes, Ph.D. thesis, Loughborough University, 1999. https://hdl.handle.net/2134/7257
[27] Nishikawa H., "Beyond Interface Gradient: A General Principle for Constructing Diffusion Schemes", AIAA 2010-5093, 2010. https://doi.org/10.2514/6.2010-5093
[28] Carlson J.-R., "Inflow/Outflow Boundary Conditions with Application to FUN3D," NASA/TM–2011-217181, 2011. https://ntrs.nasa.gov/api/citations/20110022658/downloads/20110022658.pdf
[29] Galbraith, M. C., Allmaras, S. R., and Darmofal, D. L., "SANS RANS Solutions for 3D Benchmark Configurations," AIAA 2018–1570, 2018. https://doi.org/10.2514/6.2018-1570
[30] Huang, A. C., "An Adaptive Variational Multiscale Method with Discontinuous Subscales for Aerodynamic Flows," Ph.D. thesis, Massachusetts Institute of Technology, Feb. 2020. https://dspace.mit.edu/handle/1721.1/128310
[31] Huang, A. C., Carson, H.A., Allmaras, S. R., Galbraith, M. C., Darmofal, D. L., and Kamenetskiy, D. S., "A Variational Multiscale Method with Discontinuous Subscales for Output-Based Adaptation of Aerodynamic Flows," AIAA 2020-1563, January 2020. https://doi.org/10.2514/6.2020-1563
[32] Galbraith, M. C., Allmaras, S. R., and Darmofal, D. L., "A Verification Driven Process for Rapid Development of CFD Software," AIAA 2015–818, 2015. https://doi.org/10.2514/6.2015-0818
[33] Abhyankar, S., Brown, J., Constantinescu, E. M., Ghosh, D., Smith, B. F., and Zhang, H., "PETSc/TS: A Modern Scalable ODE/DAE Solver Library," *Computing Research Repository (CoRR),*Vol.Numerical Analysis (math.NA),No. arXiv:1806.01437, 2018. http://arxiv.org/abs/1302.6066
[34] Balay, S., Abhyankar, S., Adams, M. F., Benson, S., Brown, J., Brune, P., Buschelman, K., Constantinescu, E. M., Dalcin, L., Dener A., Eijkhout, V., Faibussowitsch, J., Gropp, W. D., Hapla, V., Isaac, T., Jolivet, P., Karpeev, D., Kaushik, D., Knepley, M. G., Kong, F., Kruger, S., May, D. A., McInnes, L. C., Mills, R. T., Mitchell, L., Munson, T., Roman, J. E., Rupp, K., Sanan, P., Sarich, J., Smith, B. F., Zampini, S., Zhang, H., Zhang, H., and Zhang, J., "PETSc/TAO User's Manual," Tech.

Rep. ANL-21/39 - Revision 3.18, Argonne National Laboratory, 2022. https://petsc.org/release/docs/manual/manual.pdf

[35] Balay, S., Gropp, W. D., McInnes, L. C., and Smith, B. F., "Efficient Management of Parallelism in Object Oriented Numerical Software Libraries," *Modern Software Tools in Scientific Computing*, edited by E. Arge, A. M. Bruaset, and H. P. Langtangen, Birkhäuser Press, 1997, pp. 163–202. https://doi.org/10.1007/978-1-4612-1986-6_8

[36] Saad, Y., and Schultz, M. H., "GMRES: A Generalized Minimum Residual Algorithm for Solving Nonsymmetric Linear Systems," *SIAM Journal of Scientific and Statistical Computing*, Vol. 7, 1986, pp. 856–869. https://doi.org/10.1137/0907058

[37] Yano, M., Darmofal, D. L. "An Optimization-Based Framework for Anisotropic Simplex Mesh Adaptation," *Journal of Computational Physics*, Vol. 231, No. 22, 2012, pp. 7626–7649. https://doi.org/10.1016/j.jcp.2012.06.040

[38] Carson, H. A., Huang, A. C., Galbraith, M. C., Allmaras, S. R., Darmofal, D. L., "Mesh optimization via error sampling and synthesis: An update." AIAA 2020-0087. https://doi.org/10.2514/6.2020-0087

[39] Diskin, B., Ahmad, N., Anderson, W. K., Derlaga, J. M., Pandya, M. J., Rumsey, C. L., Wang, L., Wood, S. L., Liu, Y., Nishikawa, H., and Galbraith, M. C., "Verification Test Suite for Spalart-Allmaras QCR2000 Turbulence Model," AIAA 2021-1552, 2021. https://doi.org/10.2514/6.2021-1552

[40] Karman, S. and Wyman, N., "Automatic Unstructured Mesh Generation with Geometry Attribution," AIAA 2019-1721, 2019. https://doi.org/10.2514/6.2019-1721

[41] Lacy, D. and Clark, A. M., "Definition of Initial Landing and Takeoff Reference Configurations for the High Lift Common Research Model (CRM-HL)," AIAA 2020-2771, 2020. https://doi.org/10.2514/6.2020-2771

[42] 4th AIAA CFD High Lift Prediction Workshop, retrieved 29 November, 2022. https://hiliftpw.larc.nasa.gov/